iScience

CellPress
OPEN ACCESS

Article

# Iron atomic cluster supported on Co/NC having superior water oxidation activity over iron single atom

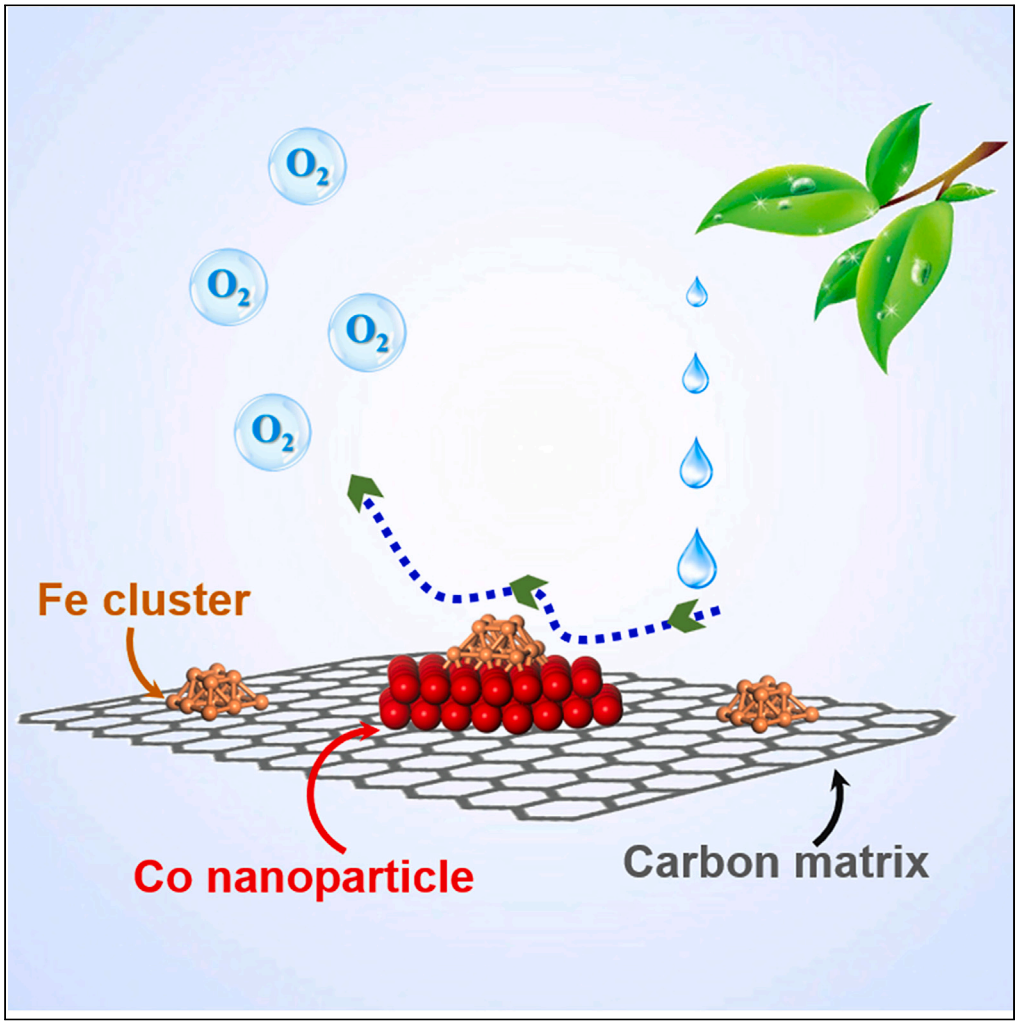


Jian Du, Yunxuan Ding, Yu Guo, Licheng Sun, Fei Li

sunlicheng@westlake.edu.cn (L.S.)
lifei@dlut.edu.cn (F.L.)

## Highlights

Fe-ACs@Co/NC and Fe-SAs@Co/NC were prepared through molecular encapsulation method

The formation of Fe-SAs or Fe-ACs depends on the size of molecular precursors

Fe-ACs@Co/NC exhibited superior OER activity over Fe-SAs@Co/NC

Du et al., iScience 26, 107339
August 18, 2023 
https://doi.org/10.1016/j.isci.2023.107339

iScience

CellPress
OPEN ACCESS

Article

# Iron atomic cluster supported on Co/NC having superior water oxidation activity over iron single atom

Jian Du,[1,2,3] Yunxuan Ding,[2,3] Yu Guo,[2,3] Licheng Sun,[1,2,3,*] and Fei Li[1,4,*]

## SUMMARY

**Carbon-supported iron-cobalt bimetallic electrocatalysts usually exhibit robust catalytic activity toward the oxygen evolution reaction (OER). However, the spatial isolation of Fe species at atomic level on cobalt-carbon solid remains a great challenge for practical catalytic applications in the OER. Here, we report the fabrication of CoFe bimetal porous carbon electrocatalysts by pyrolysis of molecularly defined iron complexes such as FePc (Pc = phthalocyanine) and $Fe(acac)_3$ pre-encapsulated in the cavities of zeolitic imidazolate framework (ZIF)-67. With this unique strategy, high-loading atomic Fe nanoclusters (Fe-ACs) and Fe single atoms (Fe-SAs) were supported on Co/NC hybrids relying on the size of the molecular Fe precursors. The former exhibited superior OER performance to the single Fe atom-decorated Co/NC, as well as other ZIF-67-derived electrocatalysts. Theoretical modulation suggests Co as the OER active site for Fe-ACs@Co/NC at the *in situ*-formed FeOOH-ACs/$Co_3O_4$ interface, while Fe was proposed as the active site for Fe-SAs@Co/NC.**

## INTRODUCTION

The oxygen evolution reaction (OER) as a half-reaction of water splitting is kinetically sluggish due to its multiple electron transfer process.[1,2] Though commercial $RuO_2$ and $IrO_2$ are well known as outstanding electrocatalysts for the OER, the large-scale application of these materials is severely constrained by their high cost and scarcity.[3–5] In this regard, the first-row transition metal-based compounds are promising alternatives. Specifically, iron (Fe)-based materials have aroused wide interests as promising OER electrocatalysts owing to the properties of nature abundance, low cost, and high intrinsic activity.[6,7] However, the poor electronic conductivity and low mass transport ability limit their catalytic performance.[8,9]

To alleviate these issues, the integration of Fe-based catalysts with conductive porous carbon materials has been considered as an effective strategy.[10–12] Zeolitic imidazolate frameworks (ZIFs) constructed by ordered arrangement of well-defined metal nodes and organic linkers have emerged as ideal precursors of heteroatom-doped porous carbons due to their optimum graphitic degree, tailorable porosity, and high specific area.[13–18] Therefore, the combination of Fe-based electrocatalysts with ZIF-derived porous carbon is believed to be a promising choice for OER, where the porous carbon matrix can not only provide accelerated electron and mass transfer pathways but also enable the exposure of more catalytic sites. Based on the previous work, the methodologies for preparing Fe-based porous carbon composites generally include either the heat treatment of Fe precursors and ZIF hosts mixture or the carbonization of Fe-doped ZIFs obtained through *in situ* ion doping.[19–21] Nevertheless, the uncontrolled agglomeration of Fe species during high-temperature pyrolysis would decrease the density of active sites, thus adversely affecting the catalytic performance. Decreasing the usage of Fe in precursors can efficiently suppress the aggregation, while the low loading of metal sites tends to cause the decline of the corresponding catalytic activity. Therefore, it remains a great challenge to uniformly disperse the Fe sites and simultaneously achieve desired OER performance.

Recently, molecularly defined Fe complexes such as iron phthalocyanine (FePc) encapsulated in the nanocages of ZIF-8 frameworks have been developed as the precursors of Fe-N-C composites via high-temperature treatment.[22] The obtained materials with single-atom Fe-N catalytic sites are highly active catalysts toward the oxygen reduction reaction (ORR) due to the atomic dispersion of Fe at a relatively high loading. As an isostructural structure to ZIF-8, ZIF-67 is also a suitable host for molecular iron complexes

[1]State Key Laboratory of Fine Chemicals, DUT-KTH Joint Education and Research Centre on Molecular Devices, Dalian University of Technology, Dalian 116024, China

[2]Center of Artificial Photosynthesis for Solar Fuels and Department of Chemistry, School of Science, Westlake University, Hangzhou 310024, China

[3]Institute of Natural Sciences, Westlake Institute for Advanced Study, Hangzhou 310024, China

[4]Lead contact

*Correspondence: sunlicheng@westlake.edu.cn (L.S.), lifei@dlut.edu.cn (F.L.)

https://doi.org/10.1016/j.isci.2023.107339

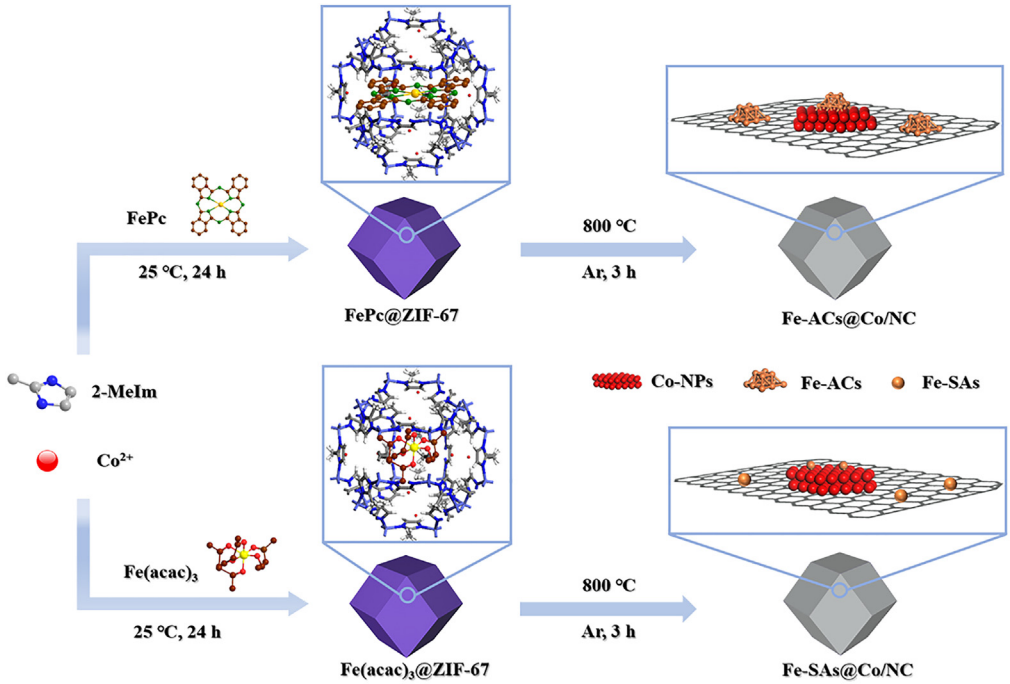


**Figure 1. Synthetic procedure of Fe-ACs@Co/NC and Fe-SAs@Co/NC.**

encapsulation; the resulting composite is envisioned as a unique precursor for Co-based N-doped porous carbon matrix decorated with highly dispersed Fe species. In addition to the structural advantages, the synergistic effect between bimetallic components of Co and Fe can further promote the OER performance. To the best of our knowledge, such a strategy for constructing ZIF-derived metal-nanocarbons has not yet been applied in the field of water oxidation electrocatalysis.

As a proof of concept, we report here the fabrication of atomically dispersed Fe clusters and atoms supported on Co nanoparticle-embedded N-doped porous carbons by means of pyrolysis of FePc and iron acetylacetonate ($Fe(acac)_3$) complexes encapsulated in ZIF-67 (Figure 1). Despite the uniform distribution of Fe in both hybrids, Fe cluster-decorated catalyst exhibits superior activity to the single-atom Fe-doped catalyst due to the Fe-Co interaction-induced relocation of the active sites for OER.

### Experimental section

The synthetic procedure is illustrated in Figure 1 (also see supporting information for details). FePc or $Fe(acac)_3$ was firstly incorporated into the nanocages of ZIF-67 by stirring with a mixture of $Co^{2+}$ and 2-methylimidazole (2-MeIm) during the crystallization. Following by carbonization at 800°C under Ar, the as-prepared nanocomposites were transformed into Fe species-decorated Co/NC hybrids. During this process, the organic ligands were converted into nitrogen-enriched carbon frameworks and the metal components were simultaneously transformed into Co nanoparticles and Fe clusters or Fe single atoms. The concentration of Fe was able to be rationally tuned by controlling the amounts of added molecular components. The optimum catalyst with regard to the OER performance was obtained with 0.4 mmol added FePc (Figure S1) or 0.3 mmol added $Fe(acac)_3$ (Figure S2). Under these conditions, the formation of Fe-ACs (Fe atomic clusters) @Co/NC from FePc@ZIF-67 and Fe-SAs (Fe single atoms) @Co/NC from $Fe(acac)_3$@ZIF-67 was identified.

## RESULTS AND DISCUSSION

### Catalyst characterization

The morphology of the FePc@ZIF-67-derived Fe-ACs@Co/NC hybrid was characterized by scanning electron microscopy (SEM). As shown in Figure 2A, Fe-ACs@Co/NC with an average size of around 1 μm well inherits the polyhedron-like shape of FePc@ZIF-67 (Figure S3), except that the surface becomes much

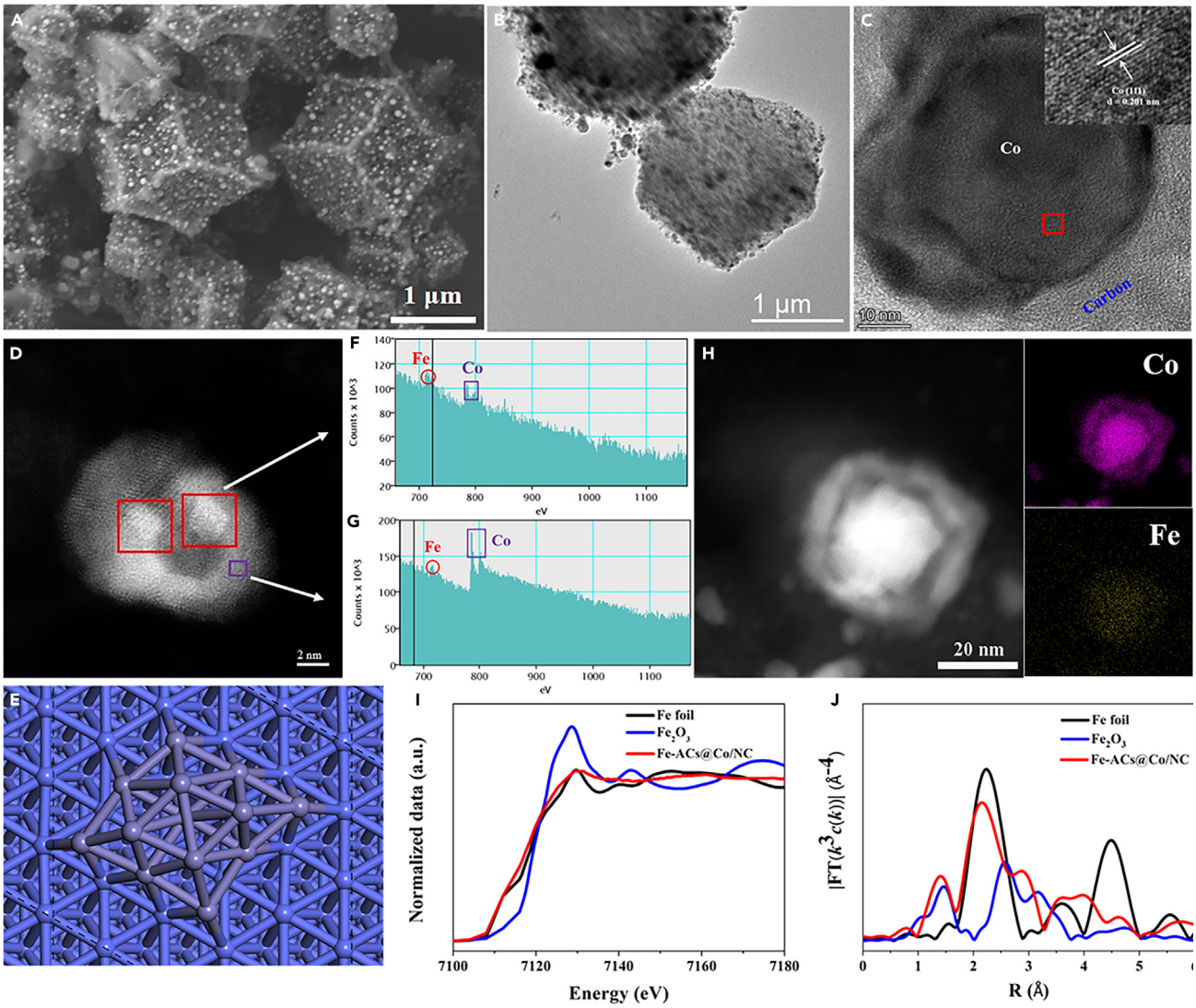


**Figure 2. The morphological and structural characterization of Fe-ACs@Co/NC**

(A–C) (A) SEM image, (B) TEM, and (C) HRTEM images of Fe-ACs@Co/NC (inset in (C): higher magnification).

(D) Cs-corrected STEM image of Fe-ACs@Co/NC. The Fe clusters are marked with red rectangles.

(E) Theoretical model of metallic Fe clusters on Co surface.

(F and G) EELS of the marked red and purple regions in Figure 1D.

(H) HAADF-STEM and the corresponding elemental mapping images of Co and Fe in Fe-ACs@Co/NC.

(I and J) (I) Fe K-edge XANES and (J) the corresponding FT-EXAFS spectra of Fe-ACs@Co/NC with $Fe_2O_3$ and Fe foil as references.

rougher. Transmission electron microscopy (TEM) in Figure 2B shows that the black metal nanoparticles are embedded in the gray carbon matrix. The high-resolution transmission electron microscopy (HRTEM) in Figure 2C clearly illustrates that metallic Co nanoparticles are wrapped by layered graphitic carbon shells with a well-defined lattice fringe of 0.201 nm. The distribution of Fe was investigated by aberration corrected scanning transmission electron microscope (Cs-corrected STEM). The bright dots with an average size of 1∼2 nm (highlighted by red rectangle) in Figures S4 and 2D demonstrate that the Fe atomic clusters are evenly dispersed on the porous carbons and Co nanoparticles. In order to investigate the elemental composition of these clusters, electron energy loss spectroscopy (EELS) was conducted in the red and purple rectangular regions in Figure 2D. Signals originated from Co and Fe were found in both regions (Figures 2F and 2G), and the relative intensity of Fe/Co signal in the red rectangular region is much higher than that in the purple region, indicating that some Fe clusters are supported on Co nanoparticles. The theoretical structure model of the Co nanoparticle-supported Fe clusters simulated from the *ab initio*

molecular dynamics (AIMD) is presented in Figure 2E, which matches well with the experimental results. The high-angle annular dark field-scanning transmission electron microscope (HAADF-STEM) image and the corresponding elemental mapping (Figure 2H) also reveal the homogeneous distribution of Co and Fe in the Fe-ACs@Co/NC structures with a Co/Fe molar ratio of 3.3: 1 (mass content of Fe: ~3.6 wt %) according to the inductively coupled plasma (ICP) atomic emission spectroscopy analysis (Table S1).

X-ray absorption fine structure (XAFS) spectroscopy was carried out to investigate the local environment of Fe in Fe-ACs@Co/NC. The Fe K-edge X-ray absorption near-edge structure (XANES) spectra (Figure 2I) reveal the near-edge absorption energy of Fe in Fe-ACs@Co/NC closely resembling that of Fe foil, indicating metallic Fe dominates the as-prepared sample. The corresponding Fourier-transformed (FT) $k^3$-weighted extended X-ray absorption fine structure (EXAFS) spectra in Figure 2J show a prominent peak at an R value of 2.15 Å for Fe-ACs@Co/NC, in agreement with the presence of Fe-Fe bonds. Compared with the reference Fe foil, no obvious peak for the second shell of Fe-Fe bond at 4.47 Å was observed, indicating the small size for the Fe clusters.[23] It is worth noting that a peak at around 1.4 Å corresponding to the Fe-O scattering paths was observed, which implies the partial oxidation of Fe clusters by exposing the sample in air. Due to the lack of the Fe-Fe bond at 2.5 Å, the formation of $Fe_2O_3$ was excluded.

Further information on the surface properties of Fe-ACs@Co/NC film was provided by X-ray photoelectron spectroscopy (XPS). The Co 2p XPS spectra in Figure S5a can be deconvoluted into three peaks in the Co $2p_{3/2}$ region at the binding energy of 778.9, 780.4, and 782.4 eV. These findings together with the observation of Co $2p_{1/2}$ peaks at 794.8, 795.9, and 797.4 eV support the existence of metallic Co nanoparticles and the oxidized surface Co species due to the exposure under air.[24–26] The Fe 2p XPS spectra shown in Figure S5b are deconvoluted into two peaks at the binding energy of 711.4 (Fe $2p_{3/2}$) and 724.4 eV (Fe $2p_{1/2}$) accompanied with two satellite peaks at 716.4 and 733.1 eV. These results prove the surface oxidation of metallic Fe clusters and agree with that obtained by the Fe EXAFS spectra.[26] In Figure S5c, the C 1s peak is fitted into two subpeaks originated from C-C bond (284.6 eV) and C-N bond (285.2 eV).[24,27] Furthermore, the N element is evidenced by the high-resolution N 1s XPS spectra in Figure S5d, which is deconvoluted into two peaks centered at 398.5 (pyridinic N) and 400.9 eV (pyrrolic N).[24]

As shown in Figures S6a–S6c, the SEM and HRTEM images of Fe-SAs@Co/NC derived from $Fe(acac)_3$@ZIF-67 suggest a similar polyhedral morphology to Fe-ACs@Co/NC. The X-ray diffraction (XRD) pattern (Figure S6d) shows two characteristic peaks at 44.2° and 51.5°, consistent with the (111) and (200) planes of metallic Co, respectively.[28,29] No Fe or FeCo nanoparticle phase formation excludes the existence of Fe aggregations in Fe-SAs@Co/NC. To clarify the form of Fe species, Cs-corrected STEM was conducted (Figures S6e and S6f), revealing the absence of observable clusters or nanoparticles on the porous carbon matrix and Co nanoparticles. On the contrary, atomically dispersed Fe atoms were clearly identified as isolated bright dots highlighted by red circles. This result is in good agreement with that for ZIF-8-encapsulated $Fe(acac)_3$, which gave rise to the isolated single-atom Fe-decorated nanocarbons by means of pyrolysis.[30] According to the ICP analysis (Table S1), the molar ratio of Co/Fe in Fe-SAs@Co/NC is around 62.3:1 (mass content of Fe: 0.53 wt %). We speculate that the structures of the detected Fe species are correlated with the sizes of the added precursors. Considering a smaller diameter of $Fe(acac)_3$ molecule (9.6 Å) than the cavity size (11.6 Å) of ZIF-67 nanocage, each $Fe(acac)_3$ molecule is assumed to be well confined and isolated by the nanocage of ZIF-67, leading to the formation of single Fe atoms at relatively low content.[30,31] In contrast, FePc with a larger molecular diameter of 14.6 Å can burst the cage of ZIF-67 along the edge direction and shorten the distance of the adjacent guest molecules.[32] To the end, the coalescence of the neighboring Fe atoms during pyrolysis leads to the formation of Fe clusters with a relatively high content. The Raman spectra in Figure S7 suggests that the intensity ratios of D- and G-bands ($I_D/I_G$) arising from N-porous carbon matrix for both Fe-SAs@Co/NC and Fe-ACs@Co/NC are 1.0, which reveals the same graphitic structure for the two samples. This phenomenon excludes the influence of the N-doped porous carbon matrix on the OER performance, and the difference in the catalytic performance of the two catalysts is only the result of the difference in the size and loading morphology of the Fe atom.

In this research, Fe-NPs (Fe nanoparticles) @Co/NC was also prepared for comparison by thermal treatment of $Fe^{2+}$-doped ZIF-67 (See supporting information for details). The resultant composite with a Co/Fe molar ratio of 4.9:1 (mass content of Fe: 6.17 wt %) was characterized by SEM, TEM, and XPS (Table S1 and Figure S8). In this sample, both Co nanoparticles and isolated Fe nanoparticles with a size of around 50 nm were evidenced by HAADF-STEM image and the corresponding elemental mapping (Figure S8e).

## Catalyst performance

To demonstrate the size effect of the different Fe precursors on catalytic performance of the derived catalysts, the electrocatalytic OER activities of Fe-ACs@Co/NC, Fe-SAs@Co/NC, and Fe-NPs@Co/NC samples were explored in a typical three-electrode system with 1 M KOH aqueous solution as electrolyte. In this setup, a glassy carbon (GC) electrode coated with the desired catalyst was used as the working electrode, Hg/HgO was used as the reference electrode, and Pt mesh as the counter electrode. The iR-corrected linear sweep voltammetry (LSV) curves of these samples were presented in Figure 3A with all potentials reported versus the reversible hydrogen electrode (RHE). Based on the polarization curves, Fe-ACs@Co/NC exhibits the highest OER activity with an overpotential of 290 mV to deliver a current density of 10 mA $cm^{-2}$, which is negatively shifted by 20 and 90 mV compared to that of Fe-SAs@Co/NC and Fe-NPs@Co/NC, respectively. As listed in Table S2, the performance obtained by Fe-ACs@Co/NC also exceeds that of other reported ZIF-67-derived catalysts supported on GC, such as FeCo-P/N ($\eta_{10}$ = 360 mV),[33] $CoNi_{0.2}Fe_{0.05}$-Z-H-P ($\eta_{10}$ = 329 mV),[34] CoP/NCNHP ($\eta_{10}$ = 310 mV),[35] and PNC/Co ($\eta_{10}$ = 370 mV).[24] In Figure 3B, Fe-ACs@Co/NC affords a lower Tafel slope of 65.9 mV $dec^{-1}$ compared with that for Fe-SAs@Co/NC (81.6 mV $dec^{-1}$) and Fe-NPs@Co/NC (117.8 mV $dec^{-1}$), indicating a favorable reaction kinetics for OER. The accelerated reaction kinetics can be also demonstrated by the electrochemical impedance spectroscopy (EIS), which were measured under an overpotential of 350 mV. Based on the Nyquist plots in Figure 3C, Fe-ACs@Co/NC has the smallest semicircle diameter among three, suggesting a lower charge transfer resistance. The double-layer capacitance ($C_{dl}$) of each electrocatalyst was calculated to determine the corresponding electrochemical active surface area (ECSA) (Figures S9a–S9c). In Figure S9d, the $C_{dl}$ values are consistent with the order of Fe-ACs@Co/NC (5.51 mF $cm^{-2}$) > Fe-SAs@Co/NC (2.88 mF $cm^{-2}$) > Fe-NPs@Co/NC (1.38 mF $cm^{-2}$), demonstrating that the atomically dispersed Fe clusters with sufficient loading bring the exposure of more active sites. When the current density was normalized to ECSA, the Fe-ACs@Co/NC still exhibits the most superior water oxidation activity with the highest current density of 0.45 mA $cm^{-2}$ under the overpotential of 350 mV (Figures S9e–S9f), which reflects its excellent intrinsic activity. The mass activities and turnover frequency (TOF) for the prepared samples measured under the overpotential of 350 mV by assuming all the metal atoms as active sites were also provided to compare their intrinsic activity. As presented in Figure 3D, the value of mass activity for Fe-ACs@Co/NC was estimated to be 0.40 A $g^{-1}$, which is about 3.64 and 30.77 times higher than that of Fe-SAs@Co/NC and Fe-NPs@Co/NC. Besides, the Fe-ACs@Co/NC catalyst exhibits the highest TOF value of 0.063 $s^{-1}$ compared with Fe-SAs@Co/NC (0.016 $s^{-1}$) and Fe-NPs@Co/NC (0.002 $s^{-1}$) (Figure 3E). The above results corporately confirm the critical role of Fe clusters in improving the intrinsic activity. In addition to the catalytic activity, Fe-ACs@Co/NC also shows long-term durability in chronopotentiometric measurement over a period of 15 h (Figure 3F).

Control experiments proved an inferior OER activity for the catalyst obtained by pyrolysis of physically mixed FePc complex and ZIF-67 (Figure S10), again highlighting the crucial role of the cage-encapsulated-precursor strategy in promoting the OER. In another experiment, FePc encapsulated in the nanocages of ZIF-8 framework (FePc@ZIF-8) was used as a precursor for Fe-ACs@NC electrocatalyst. The morphology and structure of Fe-ACs@NC were characterized as shown in Figure S11. The derived iron clusters-carbon hybrid (Fe-ACs@NC) exhibits negligible OER response with respect to Fe-ACs@Co/NC (Figure S12). The fact that either Fe-ACs@NC or Co/NC (vide supra) exhibiting low catalytic activity gives a clue to the synergy between Fe and Co in the OER.

The synergistic effect between Fe and Co for the Fe-ACs@Co/NC catalyst during OER was then confirmed by the XPS analysis. As shown in Figure S13, the two peaks in the Co $2p_{3/2}$ region for post-OER Fe-ACs@Co/NC exhibit positive shift of 0.35 and 0.45 eV when compared with those for post-OER Co/NC, respectively, indicating the modified electronic structure of Co center arising from the Fe-Co interaction. Moreover, it is found that the two peaks in Co $2p_{3/2}$ region for post-OER Fe-SAs@Co/NC only positively shift by 0.25 and 0.2 eV, respectively. The XPS results reveal that the existence of Fe clusters enables stronger Fe-Co interaction than Fe single atoms in water oxidation and such strong Fe-Co interaction can further optimize the absorption capacity for oxygen-containing intermediates, thus improving the OER performance.

## Mechanism study

To gain a deep insight into the interaction between Fe clusters and Co nanoparticles in Fe-ACs@Co/NC, density functional theory (DFT) calculations were conducted to simulate the OER process. Based on the observation of Fe clusters supported on the Co(111) surface (Figure 2D), a $Fe_{13}$ cluster on Co(111)

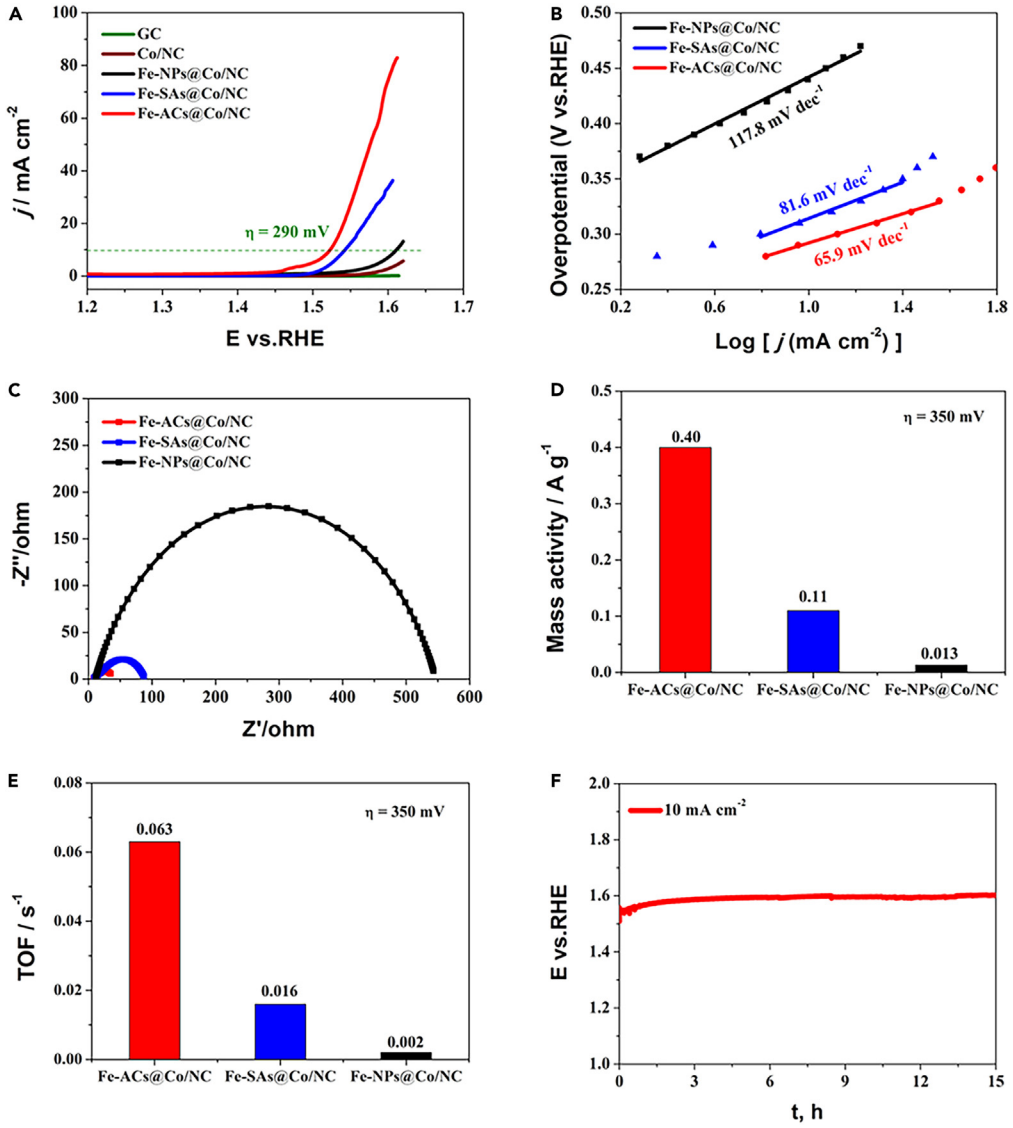


**Figure 3. Electrocatalytic OER performance of the catalysts on a glassy carbon (GC) electrode in 1 M KOH solution**

(A) LSV curves of glassy carbon (GC), Co/NC, Fe-NPs@Co/NC, Fe-SAs@Co/NC, and Fe-ACs@Co/NC corrected with iR compensation in 1 M KOH at a scan rate of 5 mV $s^{-1}$.

(B) Tafel plots of Fe-NPs@Co/NC, Fe-SAs@Co/NC, and Fe-ACs@Co/NC.

(C) EIS Nyquist plots of Fe-NPs@Co/NC, Fe-SAs@Co/NC, and Fe-ACs@Co/NC measured under an overpotential of 350 mV.

(D and E) Comparison of (D) mass activity and (E) TOF for Fe-NPs@Co/NC, Fe-SAs@Co/NC, and Fe-ACs@Co/NC measured under an overpotential of 350 mV.

(F) Chronopotentiometric test of Fe-ACs@Co/NC at 10 mA $cm^{-2}$.

surface ($Fe_{13}$/Co) was simulated by using AIMD (Figure S14), whose steady state is the same as that observed in Figure S4. With this pure metal system, the most stable adsorbed sites for the OH*, O*, and OOH* species are presumed to locate on the Fe atoms at the junction of Fe nanocluster/Co(111) surface (Figures S15a–S15d). After analyzing the energy profile of OER (Figure S15e), we are frustrated to notice that the rate determining step (RDS) of forming OOH* from O* needs an extremely high overpotential (3.58 V), which inhibits the further $O_2$ evolution. As a result, the pure metal system is prone to be oxidized by the adsorbed oxygen.

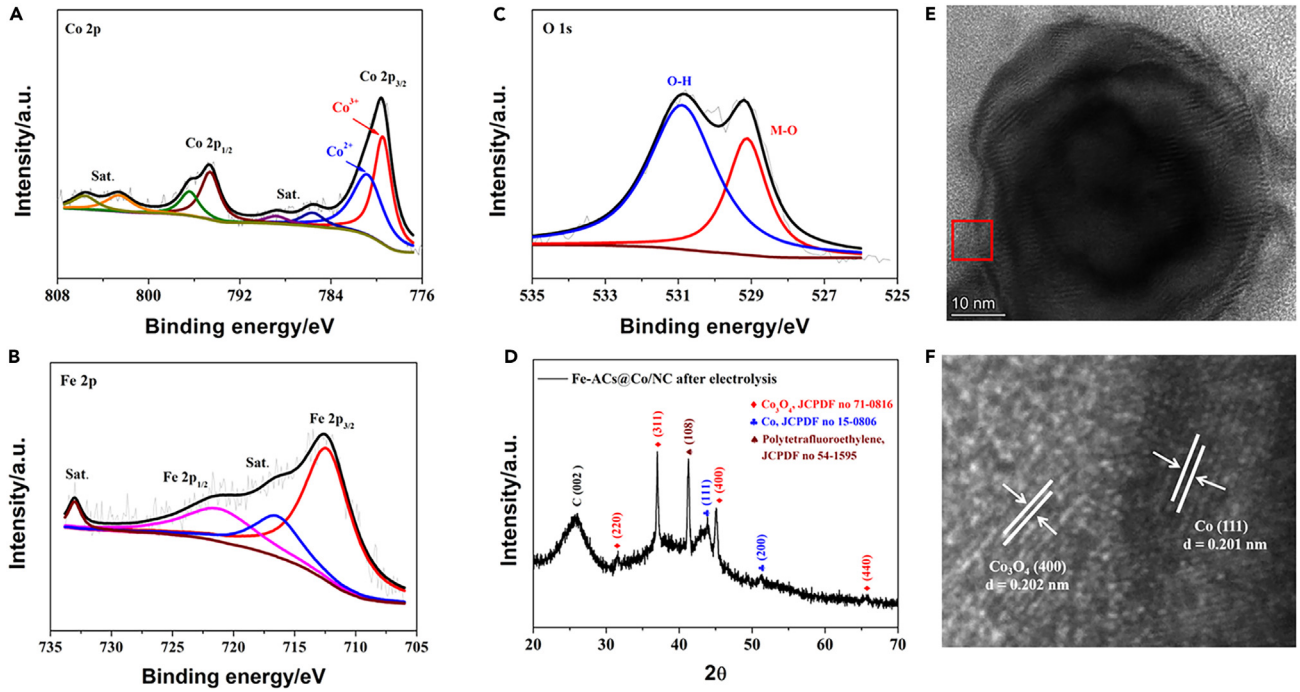


**Figure 4. Structural and morphological characterization of Fe-ACs@Co/NC after electrolysis**

(A–C) High-resolution XPS spectra of (A) Co 2p, (B) Fe 2p, and (C) O 1s of Fe-ACs@Co/NC after electrolysis.

(D) XRD pattern of Fe-ACs@Co/NC after electrolysis.

(E) TEM of Fe-ACs@Co/NC after electrolysis.

(F) The zoom-in image of the red framed region in (E).

It is thus necessary to investigate the changes in the surface compositions during OER electrolysis. After electrolysis for 10 min, the *in situ* formation of FeOOH and $Co_3O_4$ on the surfaces of Fe clusters and Co nanoparticles in Fe-ACs@Co/NC were identified based on the corresponding high-resolution XPS spectra of Co 2p, Fe 2p, and O 1s. As shown in the high-resolution Co 2p XPS spectrum in Figure 4A, the two peaks at 779.5 and 780.9 eV in Co $2p_{3/2}$ region together with two peaks appearing at 794.6 and 796.4 eV in the Co $2p_{1/2}$ region are consistent well with the $Co^{3+}$ and $Co^{2+}$ of $Co_3O_4$.[36,37] Moreover, the disappearance of metallic Co peak further confirms the surface coverage of oxidized Co species after electrolysis. The Fe $2p_{3/2}$ and Fe $2p_{1/2}$ peaks at the binding energy of 712.4 eV and 721.5 eV, respectively, in Figure 4B together with the two peaks at 529.1 and 530.9 eV in O1s XPS spectrum in Figure 4C manifest the formation of FeOOH under oxidation condition.[38] The XRD pattern of Fe-ACs@Co/NC after electrolysis in Figure 4D shows several peaks at the diffraction angle of 31.6°, 37.0°, 45.1°, and 65.5°, which correspond well to the (220), (311), (400), and (440) planes of $Co_3O_4$ (Joint Committee on Powder Diffraction File [JCPDF] no 71–0816), respectively. Furthermore, from the TEM and HRTEM images of Fe-ACs@Co/NC after electrolysis presented in Figures 4E and 4F, it is found that the lattice fringe of the inner core with an interlayer space of 0.201 nm is consistent with the (111) plane of metallic Co nanoparticle, and the appearance of the (400) lattice fringe outside the metallic Co core indicates the coverage of $Co_3O_4$ during OER process.[39]

In accordance with the above analysis, FeOOH clusters supported on $Co_3O_4$ (110) surface (FeOOH-ACs/$Co_3O_4$) were considered and computed as the potential active components for OER. Based on the differential charge density diagram in Figure 5A, the electron transfer from FeOOH to $Co_3O_4$ induces the redistribution of the electrons on the three Co sites (Co1, Co2, and Co3) at the junction of FeOOH-ACs/$Co_3O_4$, where Co1 denotes the Co site bonding with Fe site through the bridging OH from FeOOH, Co2 denotes the Co site bonding with Fe site through the bridging O from FeOOH, and Co3 denotes the Co site bonding with Fe site through the bridging O from $Co_3O_4$. Despite decreased electron density, the coordinatively saturated Fe sites result in high overpotentials (0.79 and 1.82 eV, Figure S16) for OER. On the other hand, Co1 and Co2 sites with a relatively lower electron density over that of Co3 were proposed to be more active toward OER. The OER energy profiles of FeOOH-ACs/$Co_3O_4$ in Figures 5D and S17

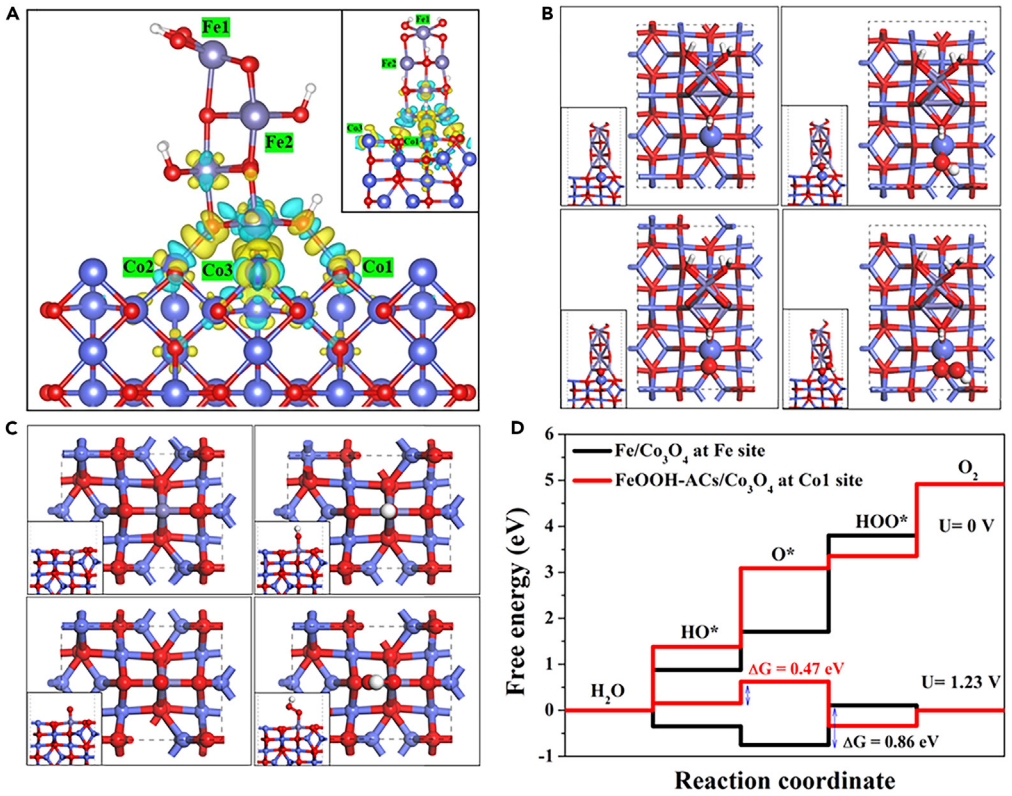


**Figure 5. Theoretical calculations at the level of density functional theory (DFT) on the electrocatalytic OER activity**

(A) Charge density difference at the junction of FeOOH cluster and $Co_3O_4$. The yellow and cyan areas represent charge accumulation and depletion, respectively, with an iso-value of 0.004 eÅ$^{-3}$. Inset shows the right view of the charge density difference diagram.

(B) Top view of the structure models of FeOOH cluster on $Co_3O_4$ (110) surface and the corresponding adsorption configurations of the OER intermediates OH*, O*, and OOH* on Co1 site. Inset shows the side view of the structure model.

(C) Top view of the structure models of $Co_3O_4$ (110) surface with doped single Fe atom and the corresponding adsorption configurations of the OER intermediates OH*, O*, and OOH* on Fe site. Inset shows the side view of the structure model.

(D) The free energy profiles of OER for Co1 site on FeOOH-ACs/$Co_3O_4$ and Fe site on Fe/$Co_3O_4$. The black and red lines represent the reaction under 0 and 1.23 V, respectively. The balls in blue, violet, red, and white represent Co, Fe, O, and H atoms, respectively.

suggest the transformation of OH* to O* as the RDS for both Co1 and Co2. In this step, an OER overpotential of 0.47 V was calculated for Co1, which is slightly lower than 0.54 V for Co2. The above results reveal that the optimized electron distribution at the couple surface can tune the absorption energy for oxygen-containing intermediates, thus improving the OER activity. The structural modes and the corresponding adsorption configurations of the reaction intermediates OH*, O*, and OOH* on Co1 are given in Figure 5B.

In comparison, the single Fe atoms in Fe-SA@Co/NC are proposed to partially replace the Co sites on $Co_3O_4$ (110) (Fe/$Co_3O_4$) due to the more favorable adsorption of reactant on Fe site. According to the geometrical models of OH*, O*, and OOH* on Fe/$Co_3O_4$ (Figure 5C), these Fe atoms are active sites for OER. The catalytic activity is restricted by the RDS of the conversion of O* to OOH* with an overpotential of 0.86 V (Figure 5D). Therefore, the theoretical results demonstrate the role of FeOOH/$Co_3O_4$ junction in the active sites location, which efficiently lowers the rate-limiting energy barrier for the OER.

## Conclusion

In summary, we have developed Fe atomic clusters- or Fe single atom-decorated Co-based N-doped porous carbon electrocatalysts for OER by means of molecular encapsulation and reduction. This strategy

enables the homogeneous dispersion of Fe species on the resulting hybrids, and the particle size of Fe is regulated with the size of the molecular precursors. As a result of size effect, the catalyst decorated with Fe atomic clusters exhibited higher OER activity and durability than the catalyst doped with Fe single atoms. Further investigation highlighted the *in situ* formation of the active FeOOH-ACs/$Co_3O_4$ junction in Fe-ACs@Co/NC, which relocates the active sites from Fe to Co atom. Given the variability and tunability of the transition metal-based molecular complexes, these findings open up a new avenue for rationally designing atomically dispersed catalysts for water splitting.

### Limitations of the study

Although the active site at the junction of *in situ* formed FeOOH-ACs/$Co_3O_4$ was determined to be Co site from theoretical calculations, the experimental proof for this point is lacking. Future research will focus on the identification of the active site by employing more experimental characterization to make the theoretical results more convincing.

## STAR★METHODS

Detailed methods are provided in the online version of this paper and include the following:

- KEY RESOURCES TABLE
- RESOURCE AVAILABILITY
  - Lead contact
  - Materials availability
  - Date and code availability
- EXPERIMENTAL MODEL AND SUBJECT DETAILS
- METHOD DETAILS
  - Materials
  - Synthesis of FePc@ZIF-67
  - Synthesis of Fe-ACs@Co/NC
  - Synthesis of FePc@ZIF-8 and Fe-ACs@NC
  - Synthesis of $Fe(acac)_3$@ZIF-67 and Fe-SAs@Co/NC
  - Synthesis of Fe@ZIF-67 and Fe-NPs@Co/NC
  - Synthesis of ZIF-67 and Co/NC
  - Material characterization
  - Preparation of electrode
  - Electrochemical measurements
  - Density functional theory (DFT) calculations
- QUANTIFICATION AND STATISTICAL ANALYSIS
- ADDITIONAL RESOURCES

## SUPPLEMENTAL INFORMATION

Supplemental information can be found online at https://doi.org/10.1016/j.isci.2023.107339.

## ACKNOWLEDGMENTS

This work was supported by the National Key R&D Program of China (2022YFA0911904), the National Natural Science Foundation of China (22088102 and 22172018), the Fundamental Research Funds for the Central Universities (DUT22QN213), and the start-up funds of Westlake University. We thank Dr. Pei Sheng, Dr Lin Liu, and Dr. Xiaohe Miao from the Instrumentation and Service Center for Physical Science (ISCPS) at Westlake University for the assistance with measurement and data interpretation. We thank Ke Wang and Yuan Cheng from the Instrumentation and Service Center for Molecular Science (ISCMS) at Westlake University for the assistance with measurement and data interpretation. We also thank Westlake University HPC Center for computation support.

## AUTHOR CONTRIBUTIONS

J.D. and Y.D. contributed equally to this work. J.D. conceived the idea, designed the present work, and carried out the experiments. Y.D. and Y.G. carried out the theoretical calculations. L.S. and F.L. supervised experiments, writing-review and editing, and funding acquisition.

## DECLARATION OF INTERESTS

The authors declare no competing interests.

## INCLUSION AND DIVERSITY

We support inclusive, diverse, and equitable conduct of research.

Received: February 8, 2023
Revised: March 6, 2023
Accepted: July 4, 2023
Published: July 16, 2023

## REFERENCES

1. Gao, L., Cui, X., Sewell, C.D., Li, J., and Lin, Z. (2021). Recent advances in activating surface reconstruction for the high-efficiency oxygen evolution reaction. Chem. Soc. Rev. *50*, 8428–8469. https://doi.org/10.1039/d0cs00962h.

2. Liu, T., Chen, Y., Hao, Y., Wu, J., Wang, R., Gu, L., Yang, X., Yang, Q., Lian, C., Liu, H., and Gong, M. (2022). Hierarchical anions at the electrode-electrolyte interface for synergized neutral water oxidation. Chem *8*, 2700–2714. https://doi.org/10.1016/j.chempr.2022.06.012.

3. Tian, L., Li, Z., Xu, X., and Zhang, C. (2021). Advances in noble metal (Ru, Rh, and Ir) doping for boosting water splitting electrocatalysis. J. Mater. Chem. A. *9*, 13459–13470. https://doi.org/10.1039/d1ta01108a.

4. Zhang, X., Zhao, Y., Zhao, Y., Shi, R., Waterhouse, G.I.N., and Zhang, T. (2019). A Simple Synthetic Strategy toward Defect-Rich Porous Monolayer NiFe-Layered Double Hydroxide Nanosheets for Efficient Electrocatalytic Water Oxidation. Adv. Energy Mater. *9*, 1900881. https://doi.org/10.1002/aenm.201900881.

5. Huang, C., Zhou, Q., Duan, D., Yu, L., Zhang, W., Wang, Z., Liu, J., Peng, B., An, P., Zhang, J., et al. (2022). Rapid self-reconstruction of iron-modified nickel hydroxysulfide for efficient and stable large-current-density water/seawater oxidation. Energy Environ. Sci. *15*, 4647–4658. https://doi.org/10.1039/d2ee01478e.

6. Feng, C., Faheem, M.B., Fu, J., Xiao, Y., Li, C., and Li, Y. (2020). Fe-Based Electrocatalysts for Oxygen Evolution Reaction: Progress and Perspectives. ACS Catal *10*, 4019–4047. https://doi.org/10.1021/acscatal.9b05445.

7. Hu, Y., Zhou, J., Li, L., Hu, Z., Yuan, T., Jing, C., Liu, R., Xi, S., Jiang, H., Wang, J.-Q., and Zhang, L. (2022). Dynamic structural transformation induced by defects in nano-rod FeOOH during electrochemical water splitting. J. Mater. Chem. A. *10*, 602–610. https://doi.org/10.1039/d1ta08938b.

8. Zhang, Y., Rui, K., Ma, Z., Sun, W., Wang, Q., Wu, P., Zhang, Q., Li, D., Du, M., Zhang, W., et al. (2018). Cost-Effective Vertical Carbon Nanosheets/Iron-Based Composites as Efficient Electrocatalysts for Water Splitting Reaction. Chem. Mater. *30*, 4762–4769. https://doi.org/10.1021/acs.chemmater.8b01699.

9. Feng, J.-X., Xu, H., Dong, Y.-T., Ye, S.-H., Tong, Y.-X., and Li, G.-R. (2016). FeOOH/Co/FeOOH Hybrid Nanotube Arrays as High-Performance Electrocatalysts for the Oxygen Evolution Reaction. Angew. Chem. Int. Ed. *55*, 3694–3698. https://doi.org/10.1002/anie.201511447.

10. Wang, H.-F., Chen, L., Wang, M., Liu, Z., and Xu, Q. (2021). Hollow Spherical Superstructure of Carbon Nanosheets for Bifunctional Oxygen Reduction and Evolution Electrocatalysis. Nano Lett *21*, 3640–3648. https://doi.org/10.1021/acs.nanolett.1c00757.

11. Zhao, J., Zhang, X., Liu, M., Jiang, Y.Z., Wang, M., Li, Z.-Y., and Zhou, Z. (2019). Metal-organic-framework-derived porous 3D heterogeneous NiFex/NiFe2O4@NC nanoflowers as highly stable and efficient electrocatalysts for the oxygen-evolution reaction. J. Mater. Chem. A. *7*, 21338–21348. https://doi.org/10.1039/c9ta08077e.

12. Feng, Y., Zhang, H., Fang, L., Mu, Y., and Wang, Y. (2016). Uniquely Monodispersing NiFe Alloyed Nanoparticles in Three-Dimensional Strongly Linked Sandwiched Graphitized Carbon Sheets for High-Efficiency Oxygen Evolution Reaction. ACS Catal *6*, 4477–4485. https://doi.org/10.1021/acscatal.6b00481.

13. Chen, Z., Hao, C., Yan, B., Chen, Q., Feng, H., Mao, X., Cen, J., Tian, Z.Q., Tsiakaras, P., and Shen, P.K. (2022). ZIF-Mg$(OH)_2$ Dual Template Assisted Self-Confinement of Small PtCo NPs as Promising Oxygen Reduction Reaction in PEM Fuel Cell. Adv. Energy Mater. *12*, 2201600. https://doi.org/10.1002/aenm.202201600.

14. Du, J., Li, F., and Sun, L. (2021). Metal–organic frameworks and their derivatives as electrocatalysts for the oxygen evolution reaction. Chem. Soc. Rev. *50*, 2663–2695. https://doi.org/10.1039/d0cs01191f.

15. Liang, Z., Kong, N., Yang, C., Zhang, W., Zheng, H., Lin, H., and Cao, R. (2021). Highly Curved Nanostructure-Coated Co, N-Doped Carbon Materials for Oxygen Electrocatalysis. Angew. Chem. Int. Ed. *60*, 12759–12764. https://doi.org/10.1002/anie.202101562.

16. Sun, T., Xu, L., Wang, D., and Li, Y. (2019). Metal organic frameworks derived single atom catalysts for electrocatalytic energy conversion. Nano Res *12*, 2067–2080. https://doi.org/10.1007/s12274-019-2345-4.

17. Hou, C.-C., Wang, H.-F., Li, C., and Xu, Q. (2020). From metal-organic frameworks to single/dual-atom and cluster metal catalysts for energy applications. Energy Environ. Sci. *13*, 1658–1693. https://doi.org/10.1039/c9ee04040d.

18. Han, X., Ling, X., Wang, Y., Ma, T., Zhong, C., Hu, W., and Deng, Y. (2019). Generation of Nanoparticle, Atomic-Cluster, and Single-Atom Cobalt Catalysts from Zeolitic Imidazole Frameworks by Spatial Isolation and Their Use in Zinc-Air Batteries. Angew. Chem. Int. Ed. *58*, 5359–5364. https://doi.org/10.1002/anie.201901109.

19. Lin, C., Wang, P., Jin, H., Zhao, J., Chen, D., Liu, S., Zhang, C., and Mu, S. (2019). An iron-doped cobalt phosphide nano-electrocatalyst derived from a metal-organic framework for efficient water splitting. Dalton Trans *48*, 16555–16561. https://doi.org/10.1039/c9dt03619a.

20. Proietti, E., Jaouen, F., Lefèvre, M., Larouche, N., Tian, J., Herranz, J., and Dodelet, J.P. (2011). Iron-based cathode catalyst with enhanced power density in polymer electrolyte membrane fuel cells. Nat. Commun. *2*, 416. https://doi.org/10.1038/ncomms1427.

21. Wang, X., Zhang, H., Lin, H., Gupta, S., Wang, C., Tao, Z., Fu, H., Wang, T., Zheng, J., Wu, G., and Li, X. (2016). Directly converting Fe-doped metal-organic frameworks into highly active and stable Fe-N-C catalysts for oxygen reduction in acid. Nano Energy *25*, 110–119. https://doi.org/10.1016/j.nanoen.2016.04.042.

22. Wang, Y., Wang, M., Zhang, Z., Wang, Q., Jiang, Z., Lucero, M., Zhang, X., Li, X., Gu, M., Feng, Z., and Liang, Y. (2019). Phthalocyanine Precursors To Construct Atomically Dispersed Iron Electrocatalysts. ACS Catal *9*, 6252–6261. https://doi.org/10.1021/acscatal.9b01617.

23. Ao, X., Zhang, W., Li, Z., Li, J.-G., Soule, L., Huang, X., Chiang, W.-H., Chen, H.M., Wang, C., Liu, M., and Zeng, X.C. (2019). Markedly Enhanced Oxygen Reduction Activity of Single-Atom Fe Catalysts via Integration with Fe Nanoclusters. ACS Nano *13*, 11853–11862. https://doi.org/10.1021/acsnano.9b05913.

24. Li, X., Niu, Z., Jiang, J., and Ai, L. (2016). Cobalt nanoparticles embedded in porous N-rich carbon as an efficient bifunctional electrocatalyst for water splitting. J. Mater. Chem. A. *4*, 3204–3209. https://doi.org/10.1039/C6TA00223D.

25. Liu, M.-R., Hong, Q.-L., Li, Q.-H., Du, Y., Zhang, H.-X., Chen, S., Zhou, T., and Zhang, J. (2018). Cobalt Boron Imidazolate Framework Derived Cobalt Nanoparticles Encapsulated in B/N Codoped Nanocarbon as Efficient Bifunctional Electrocatalysts for Overall Water Splitting. Adv. Funct. Mater. *28*, 1801136. https://doi.org/10.1002/adfm.201801136.

26. Yang, C.C., Zai, S.F., Zhou, Y.T., Du, L., and Jiang, Q. (2019). Fe3C-Co Nanoparticles Encapsulated in a Hierarchical Structure of N-Doped Carbon as a Multifunctional Electrocatalyst for ORR, OER, and HER. Adv. Funct. Mater. *29*, 1901949. https://doi.org/10.1002/adfm.201901949.

27. Xia, B.Y., Yan, Y., Li, N., Wu, H.B., Lou, X.W., and Wang, X. (2016). A metal-organic framework-derived bifunctional oxygen electrocatalyst. Nat. Energy *1*, 15006. https://doi.org/10.1038/nenergy.2015.6.

28. Gadipelli, S., Zhao, T., Shevlin, S.A., and Guo, Z. (2016). Switching effective oxygen reduction and evolution performance by controlled graphitization of a cobalt-nitrogen-carbon framework system. Energy Environ. Sci. *9*, 1661–1667. https://doi.org/10.1039/C6EE00551A.

29. Liu, S., Wang, Z., Zhou, S., Yu, F., Yu, M., Chiang, C.-Y., Zhou, W., Zhao, J., and Qiu, J. (2017). Metal–Organic-Framework-Derived Hybrid Carbon Nanocages as a Bifunctional Electrocatalyst for Oxygen Reduction and Evolution. Adv. Mater. *29*, 1700874. https://doi.org/10.1002/adma.201700874.

30. Chen, Y., Ji, S., Wang, Y., Dong, J., Chen, W., Li, Z., Shen, R., Zheng, L., Zhuang, Z., Wang, D., and Li, Y. (2017). Isolated Single Iron Atoms Anchored on N-Doped Porous Carbon as an Efficient Electrocatalyst for the Oxygen Reduction Reaction. Angew. Chem. Int. Ed. *56*, 6937–6941. https://doi.org/10.1002/anie.201702473.

31. Banerjee, R., Phan, A., Wang, B., Knobler, C., Furukawa, H., O'Keeffe, M., and Yaghi, O.M. (2008). High-Throughput Synthesis of Zeolitic Imidazolate Frameworks and Application to $CO_2$ Capture. Science *319*, 939–943. https://doi.org/10.1126/science.1152516.

32. Jiang, R., Li, L., Sheng, T., Hu, G., Chen, Y., and Wang, L. (2018). Edge-Site Engineering of Atomically Dispersed Fe-N4 by Selective C-N Bond Cleavage for Enhanced Oxygen Reduction Reaction Activities. J. Am. Chem. Soc. *140*, 11594–11598. https://doi.org/10.1021/jacs.8b07294.

33. Hong, W., Kitta, M., and Xu, Q. (2018). Bimetallic MOF-Derived FeCo-P/C Nanocomposites as Efficient Catalysts for Oxygen Evolution Reaction. Small Methods *2*, 1800214. https://doi.org/10.1002/smtd.201800214.

34. Wang, M., Dong, C.-L., Huang, Y.-C., Li, Y., and Shen, S. (2018). Electronic Structure Evolution in Tricomponent Metal Phosphides with Reduced Activation Energy for Efficient Electrocatalytic Oxygen Evolution. Small *14*, 1801756. https://doi.org/10.1002/smll.201801756.

35. Pan, Y., Sun, K., Liu, S., Cao, X., Wu, K., Cheong, W.-C., Chen, Z., Wang, Y., Li, Y., Liu, Y., et al. (2018). Core-Shell ZIF-8@ZIF-67-Derived CoP Nanoparticle-Embedded N-Doped Carbon Nanotube Hollow Polyhedron for Efficient Overall Water Splitting. J. Am. Chem. Soc. *140*, 2610–2618. https://doi.org/10.1021/jacs.7b12420.

36. Li, X., Fang, Y., Wen, L., Li, F., Yin, G., Chen, W., An, X., Jin, J., and Ma, J. (2016). $Co@Co_3O_4$ core-shell particle encapsulated N-doped mesoporous carbon cage hybrids as active and durable oxygen-evolving catalysts. Dalton Trans *45*, 5575–5582. https://doi.org/10.1039/c6dt00102e.

37. He, D., Song, X., Li, W., Tang, C., Liu, J., Ke, Z., Jiang, C., and Xiao, X. (2020). Active electron density modulation of $Co_3O_4$-based catalysts enhances their oxygen evolution performance. Angew. Chem. Int. Ed. *59*, 6929–6935. https://doi.org/10.1002/anie.202003609.

38. Fan, K., Ji, Y., Zou, H., Zhang, J., Zhu, B., Chen, H., Daniel, Q., Luo, Y., Yu, J., and Sun, L. (2017). Hollow iron-vanadium composite spheres: a highly efficient iron-based water oxidation electrocatalyst without the need for nickel or cobalt. Angew. Chem. Int. Ed. *56*, 3289–3293. https://doi.org/10.1002/anie.201611863.

39. Zhang, J., Qian, B., Sun, S., Tao, S., Chu, W., Wu, D., and Song, L. (2019). Ultrafine $Co_3O_4$ Nanoparticles within Nitrogen-Doped Carbon Matrix Derived from Metal-Organic Complex for Boosting Lithium Storage and Oxygen Evolution Reaction. Small *15*, e1904260. https://doi.org/10.1002/smll.201904260.

40. Kresse, G., and Furthmüller, J. (1996). Efficient iterative schemes for ab initio total-energy calculations using a plane-wave basis set. Phys. Rev. B *54*, 11169–11186. https://doi.org/10.1103/physrevb.54.11169.

41. Kresse, G., and Joubert, D. (1999). From ultrasoft pseudopotentials to the projector augmented-wave method. Phys. Rev. B *59*, 1758–1775. https://doi.org/10.1103/physrevb.59.1758.

42. Blöchl, P. (1994). Projector augmented-wave method. Phys. Rev. B *50*, 17953–17979. https://doi.org/10.1103/physrevb.50.17953.

43. Perdew, J.P., Burke, K., and Ernzerhof, M. (1996). Generalized gradient approximation made simple. Phys. Rev. Lett. *77*, 3865–3868. https://doi.org/10.1103/physrevlett.77.3865.

44. Huang, Z., Han, F., Li, M., Zhou, Z., Guan, X., and Guo, L. (2019). Which phase of iron oxyhydroxides (FeOOH) is more competent in overall water splitting as a photocatalyst, goethite, akaganeite or lepidocrocite? A DFT-based investigation. Comput. Mater. Sci. *169*, 109110. https://doi.org/10.1016/j.commatsci.2019.109110.

45. Liu, X., Giza, C.C., and Vrana, K.E. (1990). High-temperature x-ray diffraction study of cobalt oxide ($Co_3O_4$): Transition from normal to disordered spinel. Chem. Miner. *9*, 168–173. https://doi.org/10.1007/BF00199669.

46. Ewing, F.J. (1935). The crystal structure of lepidocrocite. J. Chem. Phys. *3*, 420–424. https://doi.org/10.1063/1.1749692.

47. Bobadova-Parvanova, P., Jackson, K.A., Srinivas, S., and Horoi, M. (2002). Density-functional investigations of the spin ordering in Fe13 clusters. Phys. Rev. B *66*, 195402. https://doi.org/10.1103/PhysRevB.66.195402.

48. Li, N., Ding, Y., Wu, J., Zhao, Z., Li, X., Zheng, Y.Z., Huang, M., and Tao, X. (2019). Efficient, full spectrum-driven $H_2$ evolution z-scheme $Co_2P$/CdS photocatalysts with Co-S bonds. ACS Appl. Mater. Interfaces *11*, 22297–22306. https://doi.org/10.1021/acsami.9b03965.

49. Song, F., Busch, M.M., Lassalle-Kaiser, B., Hsu, C.S., Petkucheva, E., Bensimon, M., Chen, H.M., Corminboeuf, C., and Hu, X. (2019). An unconventional iron nickel catalyst for the oxygen evolution reaction. ACS Cent. Sci. *5*, 558–568. https://doi.org/10.1021/acscentsci.9b00053.

50. Qiao, L., Xiao, H.Y., Meyer, H.M., Sun, J.N., Rouleau, C.M., Puretzky, A.A., Geohegan, D.B., Ivanov, I.N., Yoon, M., Weber, W.J., and Biegalski, M.D. (2013). Nature of the band gap and origin of the electro-/photo-activity of $Co_3O_4$. J. Mater. Chem. C *1*, 4628–4633. https://doi.org/10.1039/C3TC30861H.

51. Vequizo, J.J.M., and Ichimura, M. (2014). Fabrication of $Cu_2O$/γ-FeOOH heterojunction solar cells using electrodeposition. Appl. Phys. Express *7*, 045501. https://doi.org/10.7567/APEX.7.045501.

52. Singh, V., Kosa, M., Majhi, K., and Major, D.T. (2015). Putting DFT to the Test: A first-principles study of electronic, magnetic, and optical properties of $Co_3O_4$. J. Chem. Theory Comput. *11*, 64–72. https://doi.org/10.1021/ct500770m.

53. Otte, K., Schmahl, W.W., and Pentcheva, R. (2013). DFT+U study of arsenate adsorption on FeOOH surfaces: evidence for competing binding mechanisms. J. Phys. Chem. C *117*, 15571–15582. https://doi.org/10.1021/jp400649m.

## STAR★METHODS

### KEY RESOURCES TABLE

| REAGENT or RESOURCE | SOURCE | IDENTIFIER |
|---|---|---|
| Chemicals, peptides, and recombinant proteins | | |
| $Co(NO_3)_2 \cdot 6H_2O$ | Aladdin Co., Ltd | CAS:10026-22-9 |
| $FeSO_4 \cdot 7H_2O$ | Aladdin Co., Ltd | CAS: 7782-63-0 |
| $Zn(NO_3)_2 \cdot 6H_2O$ | Aladdin Co., Ltd | CAS: 10196-18-6 |
| 2-methylimidazole | Aladdin Co., Ltd | CAS: 693-98-1 |
| KOH | Aladdin Co., Ltd | CAS: 1310-58-3 |
| Iron(II) phthalocyanine | Energy Chemical | CAS: 132-16-1 |
| Iron (III) acetylacetonate | Energy Chemical | CAS: 14024-18-1 |
| $CH_3OH$ | Sigma-Aldrich | CAS: 67-56-1 |
| Nafion solution | Sigma-Aldrich | CAS: 31175-20-9 |

### RESOURCE AVAILABILITY

#### Lead contact

Further information and requests for resources should be directed to and will be fulfilled by the lead contact, Fei Li (lifei@dlut.edu.cn).

#### Materials availability

This study did not generate new unique reagents.

#### Date and code availability

- The published article includes all datasets generated or analyzed during this study.
- All data reported in this paper will be shared by the lead contact upon request.
- This paper does not report original code.
- Any additional information required to reanalyze the data reported in this paper is available from the lead contact upon request.

### EXPERIMENTAL MODEL AND SUBJECT DETAILS

This study does not use experimental models.

### METHOD DETAILS

#### Materials

Cobalt nitrate hexahydrate ($Co(NO_3)_2 \cdot 6H_2O$, 99.99%), Ferrous sulfate ($FeSO_4 \cdot 7H_2O$, 99%), Zinc nitrate hexahydrate ($Zn(NO_3)_2 \cdot 6H_2O$, 99.99%), 2-methylimidazole ($C_4H_6N_2$, 98%) and potassium hydroxide (KOH, 95%) were purchased from Aladdin chemical company. Iron(II) phthalocyanine ($C_{32}H_{16}N_8Fe$, 98%) and Iron (III) acetylacetonate ($C_{15}H_{21}FeO_6$, 99%) were purchased from Energy Chemical. Nafion solution (5wt %) was obtained from Sigma-Aldrich.

#### Synthesis of FePc@ZIF-67

FePc@ZIF-67 was synthesized according to a reported procedure with minor modification.[22] Typically, 1.16g $Co(NO_3)_2 \cdot 6H_2O$ (4 mmol) and 1.31g 2-methylimidazole (MeIM, 16 mmol) were dissolved in 60 mL of methanol solution, then 10 mL DMF solution containing 0.23g FePc (0.4 mmol) was added into the above solution followed by vigorous stirring for 24 h at room temperature. The product was subsequently separated by centrifugation and washing with methanol three times, and finally dried at 60°C for several hours.

The DMF solutions containing various amounts (0.2, 0.3 and 0.5 mmol) of FePc were used for the fabrication of FePc@ZIF-67. The resultant products were denoted as FePc@ZIF-67-2, FePc@ZIF-67-3 and FePc@ZIF-67-5, respectively.

### Synthesis of Fe-ACs@Co/NC

The obtained FePc@ZIF-67 powder was placed in a tube furnace and annealed at 800°C under Ar atmosphere with a heating rate of 5 °C $min^{-1}$ for 3 h. After naturally cooling to room temperature, the Fe-ACs@Co/NC was obtained and used directly as OER electrocatalyst without any other post-treatment.

The FePc@ZIF-67-2, FePc@ZIF-67-3 and FePc@ZIF-67-5 powders were carbonized under the same conditions described above. Based on the LSV curves shown in Figure S1, the best FePc@ZIF-67-derived catalyst was acquired with 0.4 mmol FePc as the precursor.

### Synthesis of FePc@ZIF-8 and Fe-ACs@NC

The synthetic procedure of FePc@ZIF-8 was similar to that of FePc@ZIF-67 except the replacement of $Co(NO_3)_2{\cdot}6H_2O$ with $Zn(NO_3)_2{\cdot}6H_2O$ (4 mmol, 1.19g). The resultant powder was carbonized under Ar atmosphere at the temperature of 800°C for 3 h to obtain the corresponding Fe-ACs@NC catalyst.

### Synthesis of $Fe(acac)_3$@ZIF-67 and Fe-SAs@Co/NC

The synthesis of $Fe(acac)_3$@ZIF-67 was similar to that of FePc@ZIF-67 except that FePc was replaced by $Fe(acac)_3$. In this case, the optimized amount of added $Fe(acac)_3$ is 0.3 mmol (0.11 g) (Figure S2). Fe-SAs@Co/NC was prepared with the same procedure for Fe-ACs@Co/NC.

### Synthesis of Fe@ZIF-67 and Fe-NPs@Co/NC

0.14g $FeSO_4{\cdot}7H_2O$ (0.5 mmol) and 1.02g $Co(NO_3)_2{\cdot}6H_2O$ (3.5 mmol) were dissolved into 60 mL methanol solution to form a clear solution. Then 20 mL methanol solution containing 1.31g MeIM (16 mmol) was added into the above solution. The mixture was subsequently stirred vigorously for 24 h at room temperature. The as-prepared Fe@ZIF-67 was collected by centrifugation and washing with methanol for three times, and finally dried at 60°C.

Fe-NPs@Co/NC was obtained by pyrolysis of Fe@ZIF-67 at 800°C for 3 h.

### Synthesis of ZIF-67 and Co/NC

ZIF-67 was synthesized by the direct self-assembly of $Co(NO_3)_2{\cdot}6H_2O$ (4 mmol) and MeIM (16 mmol) in methanol solution, which was subsequently transformed into Co/NC hybrid through pyrolysis at 800°C for 3 h under Ar atmosphere.

### Material characterization

The Nova NanoSEM 450 equipment was performed to observe the morphologies of the prepared samples. TEM (FEI TF30) was carried out to characterize the microstructure and lattice fringe of the prepared samples. High-angle annular dark field-scanning transmission electron microscope (HAADF-STEM) was performed on a JEM-ARM200F equipped with an aberration-corrected electron probe for the atomic resolution imaging. The crystal structures of the catalysts were determined by X-ray diffraction (XRD) patterns, which were obtained on a D/max-2400 diffractometer (Japan Rigaku Rotaflex) with Cu Kα radiation (λ = 154.1 Å). Raman spectra were collected on a Raman spectrometer (Alpha300R). The elemental composition and valence states of the samples were confirmed by X-ray photoelectron spectroscopy (XPS) (Thermo Scientific ESCALAB250). The binding energy (BE) was calibrated with respect to the C 1s peak at 284.6 eV. Inductively Coupled Plasma-Atomic Emission (ICP-AES) spectrometer (iCAP RQ, ThermoFisher) was used to quantitatively analyze the metal elements in the samples. The Co and Fe K-edge X-ray absorption near edge structure (XANES) and their extended X-ray absorption fine structure (EXAFS) experiments were performed at the beamlines 5BM-D and 20BM-B of Advanced Photon Source (APS) at Argonne National Laboratory, USA.

### Preparation of electrode

The catalyst suspension was prepared by dispersing 8 mg catalyst powder into 1 mL solution containing 0.5 mL deionized water, 0.45 mL ethanol and 0.05 mL 5% Nafion. The mixture was then ultrasonicated

for 0.5 h to form homogeneous ink. The glassy carbon (GC) with a diameter of 3 mm was polished using alumina powder on felt polishing pads prior to use. 4 μL of the catalyst ink was subsequently dropped on the surface of the GC and dried at 60°C for electrochemical tests.

## Electrochemical measurements

The electrochemical measurements were conducted on CHI 660E electrochemical Analyzer (Shanghai Chenhua Instrument Co., LTD) at room temperature by using catalyst film decorated GC as working electrode, Pt mesh and HgO/Hg electrode as counter and reference electrodes, respectively. All tests were carried out in 1 M KOH aqueous solution, and all potentials reported here were normalized to reversible hydrogen electrode (RHE) by: $E_{RHE} = E_{HgO/Hg} + 0.0592\ pH + 0.118\ V$.

Before electrochemical measurements, the working electrode was activated by electrolysis under the constant current density of 10 mA $cm^{-2}$ for 10 min. The Linear sweep voltammetry (LSV) curves corrected with iR compensation were obtained at a scan rate of 5 mV $s^{-1}$. The Tafel slopes were obtained from LSV curves by plotting overpotential against Log (current density) to assess OER kinetics. The long-term stability test was performed by continuous electrolysis under a constant current density of 10 mA $cm^{-2}$. The electrochemical impedance spectroscopy (EIS) was recorded under an overpotential of 360 mV in the frequency range from 0.01 to $10^5$ Hz with an amplitude of 5 mV. The electrochemical active surface area (ECSA) can be estimated from the double layer capacitance ($C_{dl}$) by performing CV measurements in the non-faradaic region of 1.123–1.223 V at scan rates of 20, 40, 60, 80 and 100 mV $s^{-1}$. By plotting the capacitive current density ($j_{anodic}$ -$j_{cathodic}$) against the scan rate, the value of $C_{dl}$ can be determined as half of the slope.

The value of mass activity (A $g^{-1}$) were calculated from the total loading mass of Co and Fe ($m_{Co}$+$m_{Fe}$) and the current at the overpotential of 350 mV:

$$\text{Mass activity} = \frac{i}{m_{Co}+m_{Fe}} \qquad \text{Equation 1}$$

The TOF values of catalysts deposited on glassy carbon were calculated by assuming that every metal atom is involved in the catalysis:

$$TOF = \frac{i}{4 \cdot n \cdot F} \qquad \text{Equation 2}$$

where i is the current obtained at the overpotential of 350 mV, F is the Faraday constant (96485 C $mol^{-1}$) and n is the moles of the total metal atom ($n_{Co}$+$n_{Fe}$) loaded on the electrode.

## Density functional theory (DFT) calculations

All the DFT calculations in this work were carried out using the Vienna *ab initio* simulation program (VASP).[40,41] The projector-augmented wave (PAW) method was utilized to describe the core-valence interactions,[41,42] and the plane-wave basis expansion cut-off energy was set to be 450 eV. For exchange and to correlate the functional, the generalized gradient approximation (GGA) was used with Perdew–Burke–Ernzerhof (PBE) to perform all spin-polarized calculations.[43] The equilibrium was reached when the forces on the relaxed atoms and the energies in the self-consistent iterations became less than 0.05 eV/Å and $10^{-4}$ eV, respectively. For the lattice constant optimization, the Brillouin-zone integration was sampled with 5 × 5 × 5 *k*-point for Co and $Co_3O_4$, while 6 × 2 × 8 *k*-point for lepidocrocite FeOOH.[44] The optimized lattice parameters for the bulks were a = b = c = 3.524 Å for Co, a = b = c = 8.077 Å for $Co_3O_4$, and a = 3.845 Å, b = 12.067 Å, c = 3.065 Å for FeOOH (a = b = c = 8.084 Å for $Co_3O_4$ and a = 3.87 Å, b = 12.51 Å, c = 3.06 Å for FeOOH, respectively).[45,46]

To build the Fe cluster over the Co surface, $Fe_{13}$ cluster was chosen.[47] The surfaces were modeled by using a periodic slab consisting 4-layers for a p(5 × 5) Co (111) with the 2 lower layers fixed and the 2 upper layers relaxed, and $Fe_{13}$ cluster with all atoms relaxed. A ~15 Å vacuum layer was placed on all the surface models. To thoroughly explore the most stable structures of $Fe_{13}$ cluster over the Co (111) surface, the ab-initio molecular dynamics (AIMD) was conducted at experimental temperature (300 K) for 4–5 ps with a time step of 1 fs (Figure S10).[48] A 4 × 4 × 1 Monkhorst–Pack k-point mesh sampling was used for the optimization.

The $Co_3O_4$ and FeOOH were chosen to be studied as the metal oxide system, which was consistent with experimental data. Using the pure GGA functional without Hubbard U correction,[49] the band gap of the

$Co_3O_4$ and FeOOH were 0.787 eV and 2.953 eV, which agreed well with the previous work 0.76 and 2.2 eV, respectively.[50,51] Meanwhile, the spin magnetic moments of the Co and Fe ions were 2.32 and 4.01 μB, presenting the comparable values reported before.[52,53] The $Co_3O_4$ (110) surfaces with 6-monolayers and a p(2 × 1) FeOOH (010) cluster were modeled. A p(1 × 1) $Co_3O_4$ was used for single Fe-doped model, and a p(1 × 2) $Co_3O_4$ was used for the FeOOH cluster over the surface. The Brillouin zone integrations were performed using a 3 × 4 × 1 k-point for the Fe-doped/$Co_3O_4$ and a 2 × 2 × 1 k-point for the FeOOH/$Co_3O_4$.

The four-electron reaction pathway for the OER process can be summarized as following:

$$H_2O + * \rightarrow OH^* + H^+ + e^- \quad \text{Equation 3}$$

$$OH^* \rightarrow O^* + H^+ + e^- \quad \text{Equation 4}$$

$$H_2O + O^* \rightarrow OOH^* + H^+ + e^- \quad \text{Equation 5}$$

$$OOH^* \rightarrow * + O_2 + H^+ + e^- \quad \text{Equation 6}$$

where *, OH*, O* and OOH* represent different adsorbed intermediates on the active site. For each step, the Gibbs free energy (ΔG) can be expressed as,

$$\Delta G = \Delta E + \Delta ZPE - T\Delta S - e\varphi + k_B T \ln(H^+) \quad \text{Equation 7}$$

where ΔE is the difference of the total energy between the reactants and products. ΔZPE and TΔS are the thermodynamic corrections of zero-point-energy (ZPE) and entropy (S) derived from vibrational partition function at 300 K. The $e$ is the transferred electron, the $\varphi$ is the external potential and $k_B T \ln(H^+)$ term is the free energy correction of pH. Here, all thermodynamic corrections were carried out under standard conditions (T = 300 K, pH = 0 and $\varphi$ = 0). The overpotential ($\eta$) can be determined by

$$\eta = \Delta G/e - 1.23\,V \quad \text{Equation 8}$$

## QUANTIFICATION AND STATISTICAL ANALYSIS

This study does not include statistical analysis or quantification.

## ADDITIONAL RESOURCES

This work does not include any additional resources.